

Analytical modeling of the one-dimensional power spectrum of 21-cm forest based on a halo model method

Yue Shao,¹ Tian-Yang Sun,¹ Meng-Lin Zhao,^{1,2} and Xin Zhang^{1,3,4,*}

¹*Liaoning Key Laboratory of Cosmology and Astrophysics,
College of Sciences, Northeastern University, Shenyang 110819, China*

²*Theoretical Physics Division, Institute of High Energy Physics,
Chinese Academy of Sciences, Beijing 100049, China*

³*National Frontiers Science Center for Industrial Intelligence and Systems Optimization,
Northeastern University, Shenyang 110819, China*

⁴*MOE Key Laboratory of Data Analytics and Optimization for Smart Industry,
Northeastern University, Shenyang 110819, China*

The 21-cm forest, composed of spectral absorption features from high-redshift background radio sources, provides a unique probe for studying small-scale structures during the epoch of reionization. It is particularly sensitive to detecting small-scale structures and early heating processes. Despite the rich information contained in the 21-cm forest signal, the complexity of directly modeling the signal has led to a lack of effective analytical models. However, the one-dimensional (1D) power spectrum of the 21-cm forest contains valuable information about the matter power spectrum, making analytical modeling feasible. This work employs an analytical modeling approach based on the halo model, which links the distribution of matter to dark matter halos, allowing for effective predictions of cosmic structure formation and its impact on the 21-cm signal. By considering various parameter scenarios within the halo model framework, particularly different dark matter particle masses and varying levels of cosmic heating, we can capture the complexities of small-scale structures and make the 1D power spectrum modeling applicable across a wide range of parameters. This method not only enhances our understanding of the 21-cm forest signal but also provides theoretical support for future observational data. Observing the 21-cm forest with large radio telescopes, such as the Square Kilometre Array, is anticipated to enable simultaneous exploration of dark matter properties and the heating history of the early universe.

I. INTRODUCTION

Originating from the hyperfine structure transition of neutral hydrogen atoms, the 21-cm signal constitutes a pivotal tool for investigating the first billion years of the universe including the stages of cosmic dark ages, cosmic dawn, and the epoch of reionization (EoR). During the phase when reionization is still incomplete, a significant amount of neutral hydrogen atoms accumulate within and around small-scale structures such as mini dark halos and dwarf galaxies. If the light from high-redshift radio-bright sources, such as radio-loud quasars and the radio afterglows of gamma-ray bursts, happens to traverse these structures along the line of sight, the 21-cm absorption of neutral hydrogen will produce narrow and dense absorption lines in their spectra. This phenomenon is known as the “21-cm forest” [1–7]. The absorption line characteristics of the 21-cm forest can elucidate the small-scale distribution of neutral hydrogen throughout the EoR and yield vital insights into the heating processes and the formation of small-scale structures in the early universe.

Dark matter (DM) is instrumental in the formation of cosmic structures. In contrast to the cold dark matter (CDM) model, non-CDM models, including warm dark

matter (WDM) and ultra-light dark matter, exhibit distinct behaviors on small scales [8–13]. Specifically, in the WDM model, the free-streaming of dark matter particles inhibits the formation of small-scale structures, resulting in a scarcity of dark matter halos [14–16]. Since the 21-cm forest signal is predominantly sourced by these low-mass dark matter halos, different dark matter models directly impact the abundance of 21-cm forest absorption lines [17, 18]. Furthermore, early X-ray sources in the universe heat the intergalactic medium (IGM), subsequently reducing the intensity and number of 21-cm signals [4, 18, 19]. By measuring the one-dimensional (1D) power spectrum along the line of sight, it is feasible to disentangle these two effects, as their impacts on various scales are discernible. Consequently, the 21-cm forest serves as a dual probe for exploring the properties of dark matter and the heating levels in the early universe [20].

Despite the theoretical promise of the 21-cm forest, there remains a scarcity of analytical models for this probe. Direct modeling of the 21-cm forest is intricate due to the interplay of multiple physical processes, including dark matter halo formation, gas thermal evolution, and the effects of the radiation background [2, 6, 21, 22]. Conversely, the 1D power spectrum of the 21-cm forest encapsulates extensive information about the matter power spectrum, and the analytical modeling of matter power spectra is relatively mature [23–27]. Therefore, the analytical modeling of the 1D power spectrum presents a viable approach.

* Corresponding author; zhangxin@mail.neu.edu.cn

The halo model establishes a link between the distribution of matter and dark matter halos, providing effective predictions for cosmic structure formation [28]. It has been extensively utilized in modeling the matter power spectrum, galaxy power spectrum [29, 30], and 21-cm power spectrum [31–35], among other applications. For example, prior studies have employed the halo model to simulate the 21-cm power spectrum during the cosmic dawn, where overlapping radiation flux profiles delineate the impacts of Lyman- α ($\text{Ly}\alpha$) coupling and temperature fluctuations [32–34]. Additionally, comparisons between the halo model and the semi-numerical code 21cmFAST [36] have demonstrated good agreement on large scales, with discrepancies primarily emerging at small scales. This work represents the first application of the halo model to small-scale structures, as the 21-cm forest signal at small scales harbors rich information pivotal for studying dark matter properties and cosmic heating processes. Leveraging the high frequency resolution of radio telescopes such as the Square Kilometre Array (SKA), we can capture the physical processes within small-scale structures with greater precision.

Radio-loud quasars are the most suitable background sources for detecting the 21-cm forest. Numerous studies have already predicted the number of radio-loud quasars observable at high redshifts [37, 38]. Recently, Niu et al. [39] updated the distribution of radio-loud quasars. Utilizing this updated methodology, we simulate the high-redshift radio-loud quasars observable by the SKA. We employ the halo model methodology, coupled with simulated high-redshift radio-loud quasars as background sources, to compute the 1D power spectrum of the 21-cm forest along the line of sight. We specifically consider the ramifications of different DM models (encompassing CDM and WDM) and varying heating levels (primarily X-ray heating). By juxtaposing our results with simulated data, we validate the reliability of our analytical model. This model facilitates an understanding of the perturbations in the 21-cm signal at small scales, thereby aiding in the exploration of dark matter properties and heating processes in the early universe.

II. HALO MODEL FORMALISM

A. 21-cm forest signal

The 21-cm photons emitted by high-redshift background sources are absorbed by neutral hydrogen in and around mini halos (or dwarf galaxies), generating the 21-cm forest signal. The differential brightness temperature observed for the 21-cm signal is commonly expressed as

$$\delta T_b(z) \approx \frac{T_S(z) - T_\gamma(z)}{1+z} \tau(z), \quad (1)$$

where T_S denotes the spin temperature of the HI gas and τ represents the 21-cm optical depth. T_γ is the brightness temperature of the background radiation, including the

background point source temperature T_{rad} and the cosmic microwave background (CMB) temperature T_{CMB} . The 21-cm optical depth, which quantifies the absorption strength, can be expressed in terms of the average gas properties as follows [3, 40],

$$\tau(z) \approx 0.0085[1 + \delta(z)](1+z)^{3/2} \left[\frac{x_{\text{HI}}(z)}{T_S(z)} \right] \times \left[\frac{H(z)/(1+z)}{dv_{\parallel}/dr_{\parallel}} \right] \left(\frac{\Omega_b h^2}{0.022} \right) \left(\frac{0.14}{\Omega_m h^2} \right). \quad (2)$$

Here, $\delta(z)$ is the gas overdensity, $x_{\text{HI}}(z)$ is the fraction of neutral hydrogen, $H(z)$ is the Hubble parameter, and $dv_{\parallel}/dr_{\parallel}$ is the velocity gradient along the line of sight. For the cosmological parameters, we set the values as follows: $h = 0.6736$, $\Omega_m = 0.3153$ and $\Omega_b h^2 = 0.02236$.

The observed brightness temperature of a background source, at a frequency ν , is related to the flux density $S_{\text{rad}}(\nu)$ by

$$T_{\text{rad}}(\nu, z=0) = \frac{c^2}{2k_B \nu^2} \frac{S_{\text{rad}}(\nu)}{\Omega}. \quad (3)$$

Here, c represents the speed of light, k_B is the Boltzmann constant, and Ω denotes the solid angle subtended by the telescope. The flux density $S_{\text{rad}}(\nu)$ of the background source is modeled as a power-law spectrum with a spectral index η . This model is scaled to 150 MHz, represented as $S_{\text{rad}}(\nu) = S_{150} \left(\frac{\nu}{\nu_{150}} \right)^\eta$ [41], where S_{150} represents the flux density at 150 MHz, with $\eta = -1.05$ [1].

Equations (1) and (2) reveal that the 21-cm forest signal primarily depends on the gas density, spin temperature, neutral hydrogen fraction, and velocity gradient along the line of sight. We assume $T_\gamma \gg T_S$ and T_S is assumed to be fully-coupled to the gas kinetic temperature T_K through the early $\text{Ly}\alpha$ background. T_K is determined by the heating history of the IGM, or the virial temperature of halos, depending on the gas location. For 21-cm forest observations, we only consider neutral patches, thus we can assume that $x_{\text{HI}} = 1$. We can further simplify δT_b by

$$\delta T_b(z) \approx T_0(z) \frac{1 + \delta(z)}{T_K(z)}, \quad (4)$$

where $T_0(z) = -0.0085(1+z)^{1/2} T_\gamma(z)$ is only related to the brightness temperature of the background radiation.

We utilize the 1D power spectrum along the line of sight to extract the scale dependence of the 21-cm forest signal, thereby enhancing the signal-to-noise ratio (SNR) and making the 21-cm forest an effective means [20, 41]. The 1D power spectrum of the 21-cm forest can be expressed as

$$P(k_{\parallel}, z) = T_0^2(z) P_{21}(k_{\parallel}, z), \quad (5)$$

where $P_{21}(k_{\parallel}, z)$ is the 1D power spectrum of the term $[1 + \delta(z)]/T_K(z)$, related to averaged three-dimensional

(3D) power spectrum of 21-cm signal $P_{21}(k, z)$,

$$P_{21}(k_{\parallel}, z) = \frac{1}{2\pi} \int_k^{\infty} k P_{21}(k, z) dk. \quad (6)$$

B. Halo model

Following the computation of the 1D power spectrum, we now introduce the halo model formalism used to calculate the averaged 3D power spectrum of the 21-cm forest signal. The halo model provides a framework for analytically describing the clustering of matter on both small and large scales by dividing the power spectrum into contributions from individual dark matter halos (the one-halo term) and correlations between separate halos (the two-halo term).

The averaged 3D power spectrum $P_{21}(k, z)$ consists of two components,

$$P_{21}(k, z) = P_{21}^{1h}(k, z) + P_{21}^{2h}(k, z), \quad (7)$$

where $P_{21}^{1h}(k, z)$ represents the contribution from a single halo and $P_{21}^{2h}(k, z)$ captures the contribution from two separate halos. The specific expressions for each term are given as follows,

$$\begin{aligned} P_{21}^{1h}(k, z) &= \frac{1}{\langle \rho_{21} \rangle^2} \int dM \frac{dn}{dM} |W_{21}|^2, \\ P_{21}^{2h}(k, z) &= \frac{1}{\langle \rho_{21} \rangle^2} \left[\int dM \frac{dn}{dM} |W_{21}| b \right]^2 \times P_{\text{lin}}. \end{aligned} \quad (8)$$

Here, $dn(z, M)/dM$ is the halo mass function [42, 43], $b(z, M)$ is the halo bias [44], and $P_{\text{lin}}(k, z)$ is the linear matter power spectrum. The window function $W_{21}(k, z, M)$ represents the Fourier transform of the profile $\rho_{21}(r, z, M)$, given by

$$W_{21}(k, z, M) = 4\pi \int dr r^2 \rho_{21}(r, z, M) \frac{\sin(kr)}{kr}. \quad (9)$$

The mean density profile $\langle \rho_{21}(z) \rangle$ is obtained by integrating over the halo mass function and the profile radii,

$$\langle \rho_{21}(z) \rangle = 4\pi \int dM \frac{dn(z, M)}{dM} \int dr r^2 \rho_{21}(r, z, M), \quad (10)$$

where $\rho_{21}(r, z, M)$ is the profile of $[1 + \delta(z)]/T_K(z)$, including both the density profile and the temperature profile. In the following sections, we will expand on these components, detailing the specific forms of the density and temperature profiles.

1. Halo mass function

The halo mass function is particularly crucial for modeling how these halos contribute to the 21-cm forest signal, especially for low-mass halos found in neutral regions. In the CDM model, the number density of halos

within a certain mass range at redshift z is described by the Press-Schechter formalism [42, 43]. The halo mass function is expressed as

$$\frac{dn(z, M)}{dM} = \sqrt{\frac{2}{\pi}} \frac{\bar{\rho}_{m0}}{M} \left| \frac{d\sigma(M)}{dM} \right| \frac{\delta_c(z)}{\sigma^3(M)} \exp \left[-\frac{\delta_c^2(z)}{2\sigma^2(M)} \right], \quad (11)$$

where $\bar{\rho}_{m0}$ is the current average matter density in the universe, $\sigma(M)$ is the standard deviation of the mass distribution, and $\delta_c(z)$ is the critical overdensity for collapse at redshift z .

In contrast, the WDM model shows suppressed structure formation below the free-streaming scale λ_{fs} , reflecting the thermal velocities of WDM particles. This effect leads to a decrease in the number of low-mass halos. The WDM halo mass function is approximated by [15]

$$\frac{dn(z, M)}{dM} = \frac{1}{2} \left\{ 1 + \text{erf} \left[\frac{\log_{10}(M/M_{\text{fs}})}{\sigma_{\log M}} \right] \right\} \left[\frac{dn(z, M)}{dM} \right]_{\text{PS}}, \quad (12)$$

where $\sigma_{\log M} = 0.5$ is the width of the transition and M_{fs} is the characteristic mass scale corresponding to the free-streaming scale λ_{fs} . The term $[dn(z, M)/dM]_{\text{PS}}$ is the Press-Schechter mass function from the CDM model. The free-streaming scale for WDM particles is given by [15]

$$\lambda_{\text{fs}} \approx 0.11 \left(\frac{\Omega_{\text{W}} h^2}{0.15} \right)^{1/3} \left(\frac{m_{\text{W}}}{\text{keV}} \right)^{-4/3} \text{Mpc}, \quad (13)$$

where Ω_{W} is the WDM density relative to the critical density and m_{W} is the mass of the WDM particle. Current constraints on the mass of WDM particles are typically on the order of a few keV [45–49]. Smaller WDM particle masses lead to a greater suppression scale, substantially decreasing the number of small halos and affecting the structure of the 21-cm forest signal. The Press-Schechter mass function for WDM involves modifying the CDM power spectrum to account for suppression on small scales. The matter power spectrum for WDM is given by [8]

$$P_{\text{WDM}}(k) = P_{\text{CDM}}(k) \left[(1 + (\alpha k)^{2\beta})^{-5/\beta} \right]^2, \quad (14)$$

where $\beta = 1.12$ and α is a scale factor that depends on the WDM particle mass [50],

$$\alpha = 0.049 \left(\frac{m_{\text{W}}}{\text{keV}} \right)^{-1.11} \left(\frac{\Omega_{\text{W}}}{0.25} \right)^{0.11} \left(\frac{h}{0.7} \right)^{1.22} h^{-1} \text{Mpc}. \quad (15)$$

Figure 1 illustrates the halo mass functions for CDM and WDM models at different redshifts. Since the 21-cm forest signal is mainly contributed by low-mass halos, we focus on halos with a minimum mass of $M_{\text{min}} = 10^5 M_{\odot}$, corresponding to the Jeans mass scale for the redshifts of interest. The upper mass limit, M_4 , is associated with a virial temperature of $T_{\text{vir}} = 10^4$ K. Within this mass range, the WDM model predicts fewer halos than the CDM model.

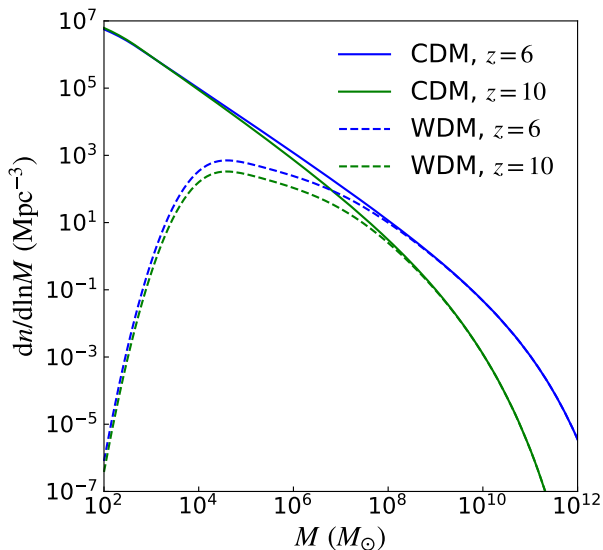


FIG. 1. Halo mass function in CDM model (solid lines) and WDM model (dashed lines) with $m_w = 6$ keV at different redshifts. The blue and green lines correspond to $z = 6$ and 10, respectively.

2. Density profile

The distribution of gas density within and around dark matter halos plays a crucial role in shaping the 21-cm absorption signal, as it directly influences the distribution of neutral hydrogen along the line of sight. For regions inside the virial radius r_{vir} , we assume that the dark matter adheres to the Navarro-Frenk-White (NFW) [51] density profile, while the gas maintains hydrostatic equilibrium with the dark matter distribution. Based on these assumptions, the gas density profile can be analytically derived as [52]

$$\ln \rho_g(r) = \ln \rho_{\text{gc}} - \frac{\mu m_p}{2k_B T_{\text{vir}}} [v_e^2(0) - v_e^2(r)], \quad (16)$$

where $\rho_g(r)$ is the gas density at distance r from the halo center, ρ_{gc} is the central gas density, μ is the mean molecular weight of the gas, m_p is the proton mass and $v_e(r)$ is the gas escape velocity at radius r . The expression for the escape velocity $v_e(r)$ is as follows,

$$v_e^2(r) = 2 \int_r^\infty \frac{GM(r')}{r'^2} dr' = 2V_c^2 \frac{F(yx) + \frac{yx}{1+yx}}{xF(y)}, \quad (17)$$

where $V_c^2 \equiv GM/r_{\text{vir}}$ is the circular velocity at the virial radius, $x = r/r_{\text{vir}}$ is the normalized radius, $F(y) = \ln(1+y) - y/(1+y)$, and G is the gravitational constant. y denotes the halo concentration parameter, which correlates with the halo mass and is commonly known as the core-halo mass relation. We utilize the fitting relationship presented in Ref. [53]. Although this relation may vary across different dark matter models, for simplicity, we apply the same core-halo mass relation across all DM models.

Due to the gravitational influence, the gas density in the surroundings of halos is enhanced. Outside the virial radius, we assume the gas density profile aligns with that of the dark matter and can be determined using the infall model [54]. The gas density profiles in and around halos of different masses are plotted in the left panel of Fig. 2.

3. Temperature profile

The temperature of the gas, especially in the neutral IGM, is vital in influencing the 21-cm absorption signal as it impacts both the spin temperature of hydrogen and the absorption strength. The temperature of the gas within the neutral IGM is mainly regulated by cosmic expansion, compton scattering with the CMB, and X-ray heating. While ultraviolet radiation primarily heats ionized regions, X-rays can deeply penetrate the neutral IGM, serving as the main heating source for the gas responsible for the 21-cm signal. The overall temperature evolution of the IGM, denoted as T_K , can be described by [55]

$$\frac{dT_K}{dt} = -2H(z)T_K + \frac{2}{3} \frac{\epsilon_{\text{comp}}}{k_B n} + \frac{2}{3} \frac{\epsilon_{\text{X,h}}}{k_B n}, \quad (18)$$

where n is the total particle number density, ϵ_{comp} is the compton heating/cooling rate per unit volume and $\epsilon_{\text{X,h}}$ is the X-ray heating rate. The term $\epsilon_{\text{X,h}}$ represents the portion of the X-ray emissivity that contributes to heating, which depends on the ionized fraction x_i . A fitting formula gives $\epsilon_{\text{X,h}} = [1 - 0.8751(1 - x_i^{0.4052})]\epsilon_{\text{X}}$ [56]. The total X-ray emissivity ϵ_{X} is proportional to the star formation rate, which is linked to the collapse rate of matter into halos. This can be written as [55]

$$\frac{2}{3} \frac{\epsilon_{\text{X}}}{k_B n H(z)} = 5 \times 10^4 \text{ K } f_{\text{X}} \left(\frac{f_{\star}}{0.1} \frac{df_{\text{coll}}/dz}{0.01} \frac{1+z}{10} \right), \quad (19)$$

where f_{\star} is the star formation efficiency, f_{coll} is the fraction of matter collapsed into atomic-cooling halos and f_{X} is a normalization factor representing the uncertain X-ray productivity in the early universe.

Within the virial radius r_{vir} , the gas kinetic temperature T_K is equated to the virial temperature T_{vir} of the halo. The virial temperature is essential for determining the ability of the gas to cool and form stars. In the regions surrounding halos, gas is adiabatically heated based on the local density, with temperature profiles increasing toward the halo center. In the regions outside the virial radius, the gas temperature is determined by a balance between adiabatic cooling due to cosmic expansion and heating from X-rays. In the presence of significant X-ray heating, the gas temperature is set by the maximum of the adiabatic temperature and the X-ray heated IGM temperature. This ensures that gas far from halos remains warmer if X-rays dominate the heating process.

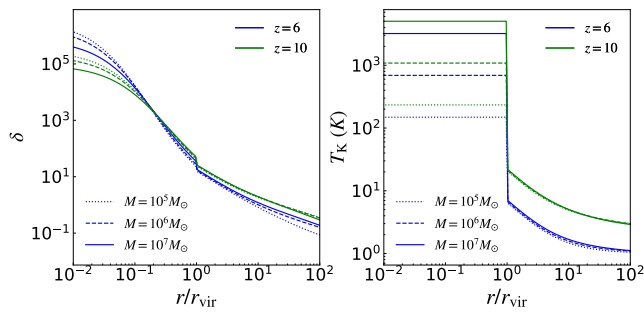


FIG. 2. The neutral hydrogen overdensity profiles (left panel) and temperature profiles (right panel) inside and outside the virial radius of a halo. In both panels, the blue and green lines correspond to $z = 6$ and 10 , respectively. The dotted, dashed and solid lines correspond to halo mass of $10^5 M_\odot$, $10^6 M_\odot$ and $10^7 M_\odot$, respectively.

The heating due to X-rays is dependent on the parameter f_X , which characterizes the efficiency of X-ray production from early sources. For higher values of f_X , the gas temperature in neutral regions is significantly raised, reducing the contrast between dense regions and the IGM in terms of their 21-cm absorption signatures. We show the temperature profiles for an un-heated IGM with different masses in the right panel of Fig. 2. According to the recent Hydrogen Epoch of Reionization Array findings [57], the temperature of IGM at redshift $z \sim 8$ is constrained within the range $15.6 \text{ K} < T_K < 656.7 \text{ K}$, corresponding to $0.02 < f_X < 0.6$. Thus for subsequent analysis, we adopt $f_X = 0.1$ as the fiducial model.

III. FORECASTS

Overall, the 1D power spectrum modeled using the halo model method is primarily influenced by the halo mass function, density profile, and temperature profile. The properties of DM and the temperature of IGM are the main factors affecting these components, corresponding to the WDM particle mass m_W and the heating level f_X . In this section, we briefly introduce the simulation of background sources. We use Bayesian analysis methods, based on the 1D power spectrum of the 21-cm forest from these background sources, to evaluate the ability of halo model to constrain m_W and f_X .

A. Radio-load quasar population

We employ the distribution of high-redshift quasars in Ref. [39] to simulate background point sources. The abundance of radio-loud quasars can be calculated as fol-

lows,

$$\frac{dn(z, F_{\text{th}})}{dzd\Omega} = \frac{dV}{dzd\Omega} D_q(z) \times \int dM \frac{dn(z, M)}{dM} \int_{R_0(M, F_{\text{th}})} dRN(R), \quad (20)$$

where $dV/dzd\Omega$ is the cosmological volume element, D_q is the duty cycle and R_0 is the threshold of radio loudness, determined from the radio flux density threshold F_{th} . $N(R)$ is the radio-loudness distribution of the radio-loud quasars,

$$N(R) = \frac{1}{\sqrt{2\pi}\sigma_0} \exp\left[-\frac{(R - \bar{R})^2}{2\sigma_0^2}\right], \quad (21)$$

where R represents radio-loudness. $\bar{R} = 2.67$ and $\sigma_0 = 0.55$ represent the best fitting parameters obtained from Ref. [39].

To calculate the survey area of SKA-LOW, we apply the following formula,

$$S_{\text{area}} = \eta \int \sin\theta d\theta \int d\phi, \quad (22)$$

where η represents the fraction of the initial survey area that remains usable for observation after excluding the Milky Way, for which we adopt a value of 0.7. Considering a declination range from 34° to -86° , the total survey area is approximately $10,000 \text{ deg}^2$.

The noise flux density observed by SKA-LOW can be estimated as [58]

$$\delta S^N \approx \frac{2k_B T_{\text{sys}}}{A_{\text{eff}} \sqrt{2\delta\nu\delta t}}, \quad (23)$$

where $\delta\nu$ is the channel width, δt is the integration time, A_{eff} is the effective collecting area of the telescope and T_{sys} is the system temperature. In our analysis, we use $\delta\nu = 1 \text{ kHz}$ and $\delta t = 100 \text{ h}$. We adopt $A_{\text{eff}}/T_{\text{sys}} = 600 \text{ m}^2 \text{ K}^{-1}$ for the SKA-LOW [59]. We consider SNR greater than 5 as the criterion for detecting quasars. Assuming an optical depth $\tau = 0.1$, to meet this criterion, we need to satisfy the condition $F_{\text{th}} \times (1 - e^{-\tau}) > 5 \times \delta S^N$.

We present the $z - S_{150}$ distribution of radio-loud quasars in Fig. 3. Assuming an integration time of $\delta t = 100 \text{ h}$ and a channel width of $\delta\nu = 1 \text{ kHz}$, under this configuration, quasars with a flux $S_{150} \gtrsim 10 \text{ mJy}$ at low redshifts between 6 and 8 can all be observed, and there are also a few quasars with a flux $S_{150} \gtrsim 100 \text{ mJy}$. As the redshift increases, only a small number of quasars with a flux above 10 mJy can be detected. Particularly, it becomes very difficult to find suitable background sources for observation at redshifts above 10. For these fainter quasars, observations can be improved by increasing the integration time or broadening the bandwidth. However, broadening the bandwidth reduces the number of measurements, which in k -space means fewer k modes, leading to increased sample variance and thus greater uncertainty in the measurements. From these, we select 10 radio-loud quasars with significant flux densities at different redshifts for further analysis.

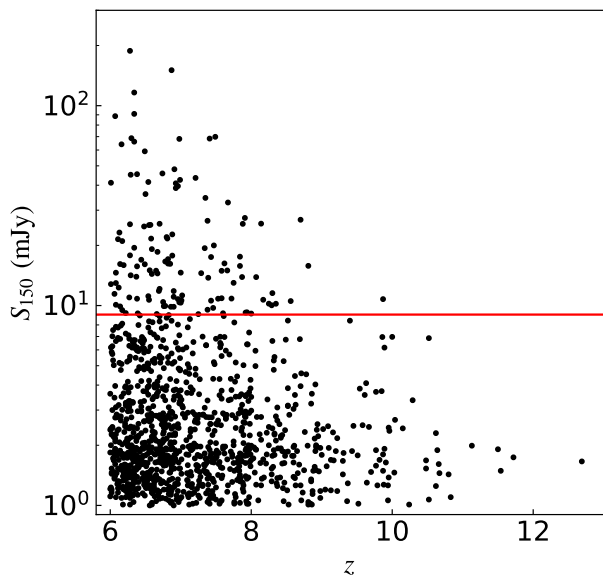


FIG. 3. Simulated radio-loud quasar distribution with SKA-LOW. The red line represents the flux threshold that SKA-LOW can observe.

B. Parameter estimation

The observational uncertainties in the 21-cm forest include the thermal noise and the sample variance. The thermal noise uncertainty for the 1D power spectrum is given by [41]

$$P^N = \frac{1}{\sqrt{N_s}} \left(\frac{\lambda_z^2 T_{\text{sys}}}{A_{\text{eff}} \Omega} \right)^2 \left(\frac{\Delta r_z}{2 \Delta \nu_z \delta t_{0.5}} \right), \quad (24)$$

where N_s is the number of neutral segments measured, $\Delta \nu_z$ is the total observing bandwidth corresponding to Δr_z , $\delta t_{0.5}$ is half of the integration time. In actual observations of the 21-cm forest signal, we can divide the total observation time into two parts and perform cross-correlation on the signals observed in these two segments. This approach helps to reduce the thermal noise. Similarly, in our work, we employed this method to estimate the thermal noise. We utilize $P(k_{\parallel}, z)$ to estimate the sample variance, and the total measurement error of the 1D power spectrum σ_P is

$$\sigma_P = \frac{1}{\sqrt{N_m}} [P^N + P(k_{\parallel}, z)], \quad (25)$$

where N_m is the number of k modes, which includes the number of source spectra segment and the number of k modes in each k bin.

Due to current observations only placing a lower limit on m_W , we employ Bayesian analysis to deduce its reciprocal during the inference process. We employed Bilby [60] for Bayesian analysis to estimate the parameters f_X and m_W^{-1} . For the observed 1D power spectrum \tilde{P} , it can

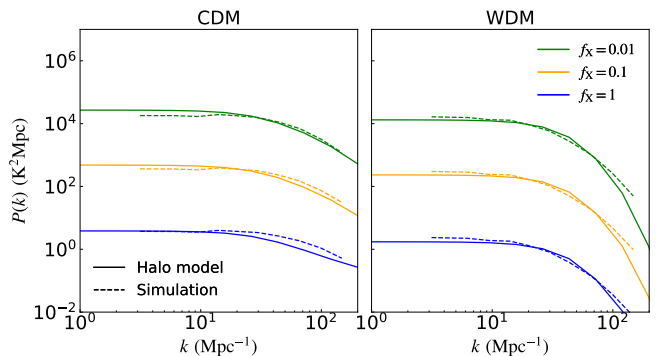


FIG. 4. Comparison of the 21-cm forest halo model presented in this paper (solid curves) with the simulation results (dashed curves) at $z = 9$, assuming a flux density of $S_{150} = 10$ mJy. The green, yellow and blue curves correspond to $f_X = 0.01, 0.1$ and 1, respectively. The left and right panels represent CDM model and WDM model with $m_W = 6$ keV, respectively.

be expressed as

$$\mathcal{P}(f_X, m_W^{-1} | \tilde{P}) = \frac{\mathcal{P}(\tilde{P} | f_X, m_W^{-1}) \mathcal{P}(f_X, m_W^{-1})}{\mathcal{P}(\tilde{P})}, \quad (26)$$

where $\mathcal{P}(f_X, m_W^{-1} | \tilde{P})$ is the posterior distribution, $\mathcal{P}(\tilde{P} | f_X, m_W^{-1})$ is the likelihood function, $\mathcal{P}(f_X, m_W^{-1})$ is the prior distribution, and $\mathcal{P}(\tilde{P})$ is the normalization constant. The likelihood function for the 1D power spectrum $\tilde{P}_{i,k}$, based on the i -th observation and the k -th bin, is defined as follows:

$$\mathcal{P}(\tilde{P} | f_X, m_W^{-1}) = \prod_{i,k} \frac{1}{\sqrt{2\pi\sigma_{\tilde{P}_{i,k}}^2}} \exp \left[-\frac{(\tilde{P}_{i,k} - P_{i,k})^2}{2\sigma_{\tilde{P}_{i,k}}^2} \right], \quad (27)$$

where $\sigma_{\tilde{P}_{i,k}}$ is the measurement error. The prior distributions for the parameters f_X and m_W^{-1} are uniform distributions over the range $[0.01, 1]$ and $[1/9, 1/3]$ keV $^{-1}$. We used the Markov Chain Monte Carlo [61] sampling algorithm to draw samples from the posterior distribution, estimating the parameters f_X and m_W^{-1} and their precision.

IV. RESULTS AND DISCUSSION

While the DM model and heating effects suppress the 21-cm forest signal, their impacts on different scales vary significantly. These differences can be revealed through the 1D power spectrum. To elucidate these scale-dependent effects, we developed an analytical model for the 1D power spectrum of the 21-cm forest using the halo model method and conducted detailed calculations of the 1D power spectra under various DM models and heating levels. We consider a distance of 2 comoving Mpc along the line of sight, corresponding to a bandwidth of

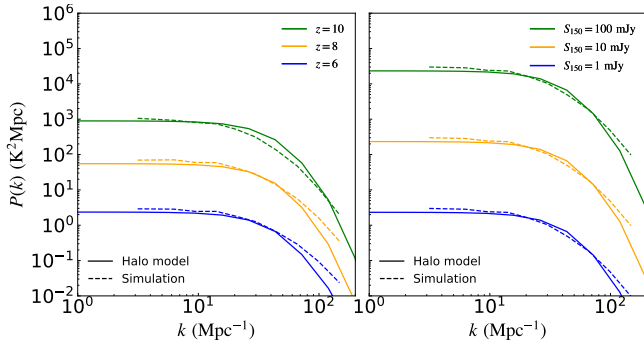


FIG. 5. Comparison between the 21-cm forest halo model in this paper (solid curves) and the simulation results (dashed curves). The blue, yellow and green curves in left panel correspond to $z = 6, 8$ and 10 , respectively, with $S_{150} = 10$ mJy. The green, yellow and blue curves in right panel correspond to $S_{150} = 100$ mJy, 10 mJy and 1 mJy, respectively, at $z = 9$.

$\Delta v_z = 0.11$ MHz and $k_{\min} = 3.14$ Mpc $^{-1}$ at $z = 10$. Here, we only consider modeling on small scales below 2 Mpc for comparison with the simulation result. Additionally, modeling on larger scales would involve considering the ionized fraction, which would add complexity to the model.

For a direct comparison between our analytical model and the simulated 1D power spectra from previous studies, we conducted small-scale simulations on grids of 2 Mpc in length [20]. Each $(2 \text{ Mpc})^3$ grid is populated with halos based on the conditional halo mass function for the CDM or WDM [28, 62]. The initial density is the mean density of the universe. The density in each voxel is determined by the NFW profile or the infall model profile. The gas temperature within each voxel is determined by its location relative to halos and the thermal history of the universe. The large-scale reionization history only determines the probability of encountering a neutral patch of the IGM of a certain length along the line of sight, and we focus only on neutral regions on small scales. Each grid is divided into 500^3 voxels, and we average over 500^2 lines along the line of sight direction to obtain the final 1D power spectrum for comparison with the analytical model, thereby mitigating the impact of sample variance.

In Fig. 4, we present a comparison between the 21-cm forest halo model developed in this work and the simulation results obtained using methods from Ref. [20]. We display the results for both the CDM model (left panel) and the WDM model (right panel) at different heating levels, with fixed redshift $z = 9$ and $S_{150} = 10$ mJy. Our analytical model shows good agreement with simulation results across various DM models and different levels of X-ray heating. It is noteworthy that, at such small scales, the one-halo term dominates the 1D power spectrum. Therefore, we only present the results for the one-halo term.

We fix $m_W = 6$ keV and $f_X = 0.1$ as the fiducial model, and calculate the performance of the 21-cm forest halo model at different redshifts and with different

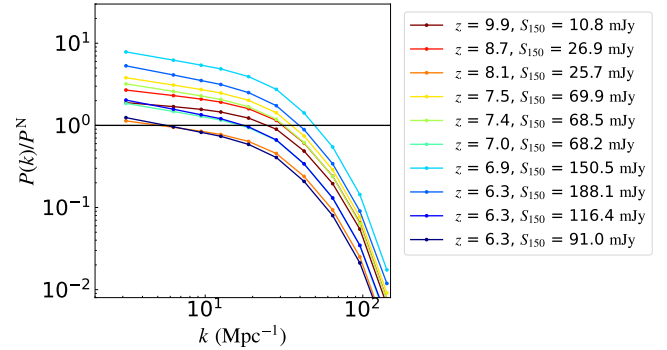


FIG. 6. The SNR, $P(k)/P^N$, of the 21-cm forest calculated from 10 radio-loud quasars. Each quasar has 10 segments along the line of sight and an observation time of $\delta t = 100$ h.

background source flux densities in Fig. 5. The left panel shows the results for redshifts $z = 6, 8$ and 10 , assuming a uniform flux density $S_{150} = 10$ mJy for consistency. Note that in practice, at low redshifts, many quasars can have a flux density exceeding 10 mJy, whereas at high redshifts, such quasars are relatively few. The right panel fixes the redshift $z = 9$ and calculates the results for different background source flux densities $S_{150} = 1$ mJy, 10 mJy and 100 mJy. This indicates that our model is applicable across a wide range of parameter space.

To accurately describe the heating history of the universe and constrain the heating level f_X , we selected 10 quasars, each with 10 segments, at different redshifts. The SNRs of the 1D power spectra of the 21-cm forest for these quasars are shown in Fig. 6. Considering that thermal noise varies with redshift, we present the SNR, $P(k)/P^N$. At higher redshifts, the temperature of the IGM is lower, which means that quasars can achieve sufficient SNR even with moderate flux densities. In contrast, at lower redshifts, quasars need to be brighter to attain the same level of SNR. Quasars at redshifts between 7 and 8 are particularly well-suited for observations of the 1D power spectrum of the 21-cm forest.

At the end of the EoR, the neutral hydrogen fraction of the universe is already quite low, and most of the universe at $z \sim 6$ has been ionized. However, since the lengths of the segments we are considering are very short, only about 2 Mpc, it is still possible to have up to ten segments of neutral regions. Additionally, for quasars at higher redshifts, there may be many more neutral segments. To simplify, we assume that each quasar has 10 segments, totaling 100 segments. We take the redshift of the quasars as the redshift of the 21-cm forest signal and assume that the quasars do not produce a heating effect.

We applied the Bayesian methods to constrain the parameters m_W and f_X , which are presented in Fig. 7. Based on the prospective observations with SKA-LOW, we assumed 100 h of observation for each quasar, accumulating to a total of 1000 h of observational time. We adopted a fiducial model with $m_W = 6$ keV and $f_X = 0.1$, and calculated the absolute errors for the parameters to

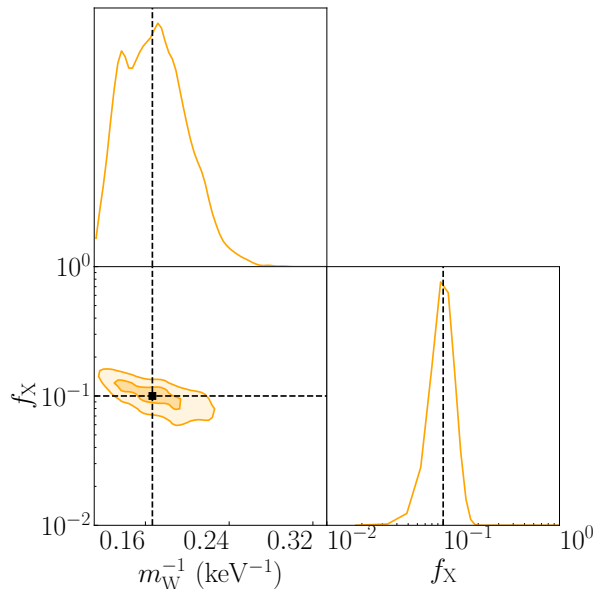


FIG. 7. Bayesian constraints at the 68.3% and 95.4% confidence levels for the parameters f_X and m_W , derived from the 1D power spectrum of the 21-cm forest observed with SKA-LOW.

be $\sigma_{m_W} = 1.3$ keV and $\sigma_{f_X} = 0.02$. By combining 21-cm forest data from various redshifts, we can effectively constrain the mass of WDM particles and trace the evolution of the cosmic thermal history, thereby revealing the formation of the first galaxies.

Here, we employ Bayesian methods as they offer distinct advantages over Fisher matrix analysis in handling complex probability distributions and the nonlinear nature of 1D power spectrum data. Furthermore, potential non-Gaussian features within the 21-cm data can be addressed by incorporating more complex likelihood functions or deep learning approaches [63] to capture intricate patterns in the data.

Observing the 21-cm forest is contingent upon high-redshift, radio-bright background sources, with radio-loud quasars and radio afterglows of gamma-ray bursts emerging as the most viable options. As some of the brightest objects in the universe, quasars' radio emissions can serve as the background for the 21-cm forest. In particular, radio-loud quasars provide sufficient intensity for observing the 21-cm signal. Using the quasar luminosity function, it is possible to predict the number of quasars, and in the SKA era, it is expected that a sufficient number of quasars will be detected to serve as background

sources for the 21-cm forest [37, 64–66]. Some models have suggested that although the abundance of radio-loud quasars at high redshifts is low, it is still adequate to support 21-cm forest studies [38, 39].

V. CONCLUSION

In this work, we propose an innovative analytical modeling approach, using the halo model method for the first time to theoretically modeling the 1D power spectrum of the 21-cm forest. This method not only addresses the lack of analytical models for the 21-cm forest but also significantly reduces the need for simulations. By comparing our model with the results from commonly used small-scale simulation methods for the 21-cm forest, we find that our model exhibits high consistency with the simulation results across a wide range of parameter spaces. This consistency not only validates the effectiveness of our model but also demonstrates its universality under different parameter conditions.

The 21-cm forest signal primarily comes from the neutral hydrogen within and around halos, so we focus on small-scale modeling. However, modeling at larger scales is also important. For high-redshift radio point sources, the neutral segments in their light paths are numerous and long, making 2 Mpc scale modeling inadequate. For low-redshift radio point sources, modeling at larger scales requires considering the ionized fraction of neutral hydrogen, which helps explore the evolution of the reionization history.

By incorporating effects such as ionization fluctuations and $\text{Ly}\alpha$ coupling, the halo model method can also be applied to larger scales. Alternatively, other possible analytical models can be developed [67, 68]. With the help of these analytical models, future studies related to the 21-cm forest can more accurately predict and interpret observational data, making the 21-cm forest a reliable probe for studying small-scale structures in the early universe. This probe will not only help us better understand the nature of dark matter but also reveal the heating history of the early universe.

ACKNOWLEDGMENTS

We thank Yichao Li and Yidong Xu for helpful discussions. This work was supported by the National SKA Program of China (grant Nos. 2022SKA0110200 and 2022SKA0110203), the National Natural Science Foundation of China (grant Nos. 12473001, 11975072, 11875102, and 11835009), and the National 111 Project (Grant No. B16009).

[1] C. Carilli, N. Y. Gnedin, and F. Owen, *Astrophys. J.* **577**, 22 (2002), [arXiv:astro-ph/0205169](https://arxiv.org/abs/astro-ph/0205169).

[2] S. Furlanetto and A. Loeb, *Astrophys. J.* **579**, 1 (2002), [arXiv:astro-ph/0206308](https://arxiv.org/abs/astro-ph/0206308).

- [3] S. Furlanetto, *Mon. Not. Roy. Astron. Soc.* **370**, 1867 (2006), [arXiv:astro-ph/0604223](#).
- [4] Y. Xu, X. Chen, Z. Fan, H. Trac, and R. Cen, *Astrophys. J.* **704**, 1396 (2009), [arXiv:0904.4254 \[astro-ph.CO\]](#).
- [5] Y. Xu, A. Ferrara, F. S. Kitaura, and X. Chen, *Sci. China Phys. Mech. Astron.* **53**, 1124 (2010), [arXiv:1002.4356 \[astro-ph.CO\]](#).
- [6] Y. Xu, A. Ferrara, and X. Chen, *Mon. Not. Roy. Astron. Soc.* **410**, 2025 (2011), [arXiv:1009.1149 \[astro-ph.CO\]](#).
- [7] B. Ciardi *et al.*, *Mon. Not. Roy. Astron. Soc.* **428**, 1755 (2013), [arXiv:1209.2615 \[astro-ph.CO\]](#).
- [8] P. Bode, J. P. Ostriker, and N. Turok, *Astrophys. J.* **556**, 93 (2001), [arXiv:astro-ph/0010389](#).
- [9] D. J. E. Marsh, (2016), [arXiv:1605.05973 \[astro-ph.CO\]](#).
- [10] J. B. Muñoz, C. Dvorkin, and F.-Y. Cyr-Racine, *Phys. Rev. D* **101**, 063526 (2020), [arXiv:1911.11144 \[astro-ph.CO\]](#).
- [11] D. Jones, S. Palatnick, R. Chen, A. Beane, and A. Lidz, *Astrophys. J.* **913**, 7 (2021), [arXiv:2101.07177 \[astro-ph.CO\]](#).
- [12] E. G. M. Ferreira, *Astron. Astrophys. Rev.* **29**, 7 (2021), [arXiv:2005.03254 \[astro-ph.CO\]](#).
- [13] X. Shen *et al.*, (2023), [arXiv:2304.06742 \[astro-ph.GA\]](#).
- [14] V. Avila-Reese, P. Colin, O. Valenzuela, E. D’Onghia, and C. Firmani, *Astrophys. J.* **559**, 516 (2001), [arXiv:astro-ph/0010525](#).
- [15] R. E. Smith and K. Markovic, *Phys. Rev. D* **84**, 063507 (2011), [arXiv:1103.2134 \[astro-ph.CO\]](#).
- [16] A. Schneider, R. E. Smith, and D. Reed, *Mon. Not. Roy. Astron. Soc.* **433**, 1573 (2013), [arXiv:1303.0839 \[astro-ph.CO\]](#).
- [17] M. Sitwell, A. Mesinger, Y.-Z. Ma, and K. Sigurdson, *Mon. Not. Roy. Astron. Soc.* **438**, 2664 (2014), [arXiv:1310.0029 \[astro-ph.CO\]](#).
- [18] H. Shimabukuro, K. Ichiki, S. Inoue, and S. Yokoyama, *Phys. Rev. D* **90**, 083003 (2014), [arXiv:1403.1605 \[astro-ph.CO\]](#).
- [19] K. J. Mack and J. S. B. Wyithe, *Mon. Not. Roy. Astron. Soc.* **425**, 2988 (2012), [arXiv:1101.5431 \[astro-ph.CO\]](#).
- [20] Y. Shao, Y. Xu, Y. Wang, W. Yang, R. Li, X. Zhang, and X. Chen, *Nature Astron.* **7**, 1116 (2023), [arXiv:2307.04130 \[astro-ph.CO\]](#).
- [21] T. Šoltinský, J. S. Bolton, N. Hatch, M. G. Haehnelt, L. C. Keating, G. Kulkarni, E. Puchwein, J. Chardin, and D. Aubert, *Mon. Not. Roy. Astron. Soc.* **506**, 5818 (2021), [arXiv:2105.02250 \[astro-ph.CO\]](#).
- [22] T. Šoltinský, J. S. Bolton, M. Molaro, N. Hatch, M. G. Haehnelt, L. C. Keating, G. Kulkarni, and E. Puchwein, (2022), [10.1093/mnras/stac3710, arXiv:2211.07655 \[astro-ph.CO\]](#).
- [23] C.-P. Ma and J. N. Fry, *Astrophys. J.* **543**, 503 (2000), [arXiv:astro-ph/0003343](#).
- [24] R. E. Smith, J. A. Peacock, A. Jenkins, S. D. M. White, C. S. Frenk, F. R. Pearce, P. A. Thomas, G. Efstathiou, and H. M. P. Couchmann (VIRGO Consortium), *Mon. Not. Roy. Astron. Soc.* **341**, 1311 (2003), [arXiv:astro-ph/0207664](#).
- [25] A. Mead, J. Peacock, C. Heymans, S. Joudaki, and A. Heavens, *Mon. Not. Roy. Astron. Soc.* **454**, 1958 (2015), [arXiv:1505.07833 \[astro-ph.CO\]](#).
- [26] O. H. E. Philcox, D. N. Spergel, and F. Villaescusa-Navarro, *Phys. Rev. D* **101**, 123520 (2020), [arXiv:2004.09515 \[astro-ph.CO\]](#).
- [27] A. Acuto, I. G. McCarthy, J. Kwan, J. Salcido, S. G. Stafford, and A. S. Font, *Mon. Not. Roy. Astron. Soc.* **508**, 3519 (2021), [arXiv:2109.11855 \[astro-ph.CO\]](#).
- [28] A. Cooray and R. K. Sheth, *Phys. Rept.* **372**, 1 (2002), [arXiv:astro-ph/0206508](#).
- [29] U. Seljak, *Mon. Not. Roy. Astron. Soc.* **318**, 203 (2000), [arXiv:astro-ph/0001493](#).
- [30] S. G. Murray, B. Diemer, Z. Chen, A. G. Neuhold, M. A. Schnapp, T. Peruzzi, D. Blevins, and T. Engelman, *Astron. Comput.* **36**, 100487 (2021), [arXiv:2009.14066 \[astro-ph.CO\]](#).
- [31] C. Feng, A. Cooray, and B. Keating, *Astrophys. J.* **846**, 21 (2017), [arXiv:1701.07005 \[astro-ph.CO\]](#).
- [32] A. Schneider, S. K. Giri, and J. Mirocha, *Phys. Rev. D* **103**, 083025 (2021), [arXiv:2011.12308 \[astro-ph.CO\]](#).
- [33] A. Schneider, T. Schaeffer, and S. K. Giri, *Phys. Rev. D* **108**, 043030 (2023), [arXiv:2302.06626 \[astro-ph.CO\]](#).
- [34] T. Schaeffer, S. K. Giri, and A. Schneider, (2023), [10.1093/mnras/stad2937, arXiv:2305.15466 \[astro-ph.CO\]](#).
- [35] P. Hitz, P. Berner, D. Crichton, J. Hennig, and A. Refregier, (2024), [arXiv:2410.01694 \[astro-ph.CO\]](#).
- [36] A. Mesinger, S. Furlanetto, and R. Cen, *Mon. Not. Roy. Astron. Soc.* **411**, 955 (2011), [arXiv:1003.3878 \[astro-ph.CO\]](#).
- [37] Z. Haiman, E. Quataert, and G. C. Bower, *Astrophys. J.* **612**, 698 (2004), [arXiv:astro-ph/0403104](#).
- [38] A. J. Gloudemans, K. J. Duncan, H. J. A. Röttgering, T. W. Shimwell, B. P. Venemans, P. N. Best, M. Brüggén, G. Calistro Rivera, A. Drabent, M. J. Hardcastle, G. K. Miley, D. J. Schwarz, A. Saxena, D. J. B. Smith, and W. L. Williams, *Astron. Astrophys.* **656**, A137 (2021), [arXiv:2110.06222 \[astro-ph.GA\]](#).
- [39] Q. Niu, Y. Li, Y. Xu, H. Guo, and X. Zhang, (2024), [arXiv:2407.18136 \[astro-ph.CO\]](#).
- [40] P. Madau, A. Meiksin, and M. J. Rees, *Astrophys. J.* **475**, 429 (1997), [arXiv:astro-ph/9608010](#).
- [41] N. Thyagarajan, *Astrophys. J.* **899**, 16 (2020), [arXiv:2006.10070 \[astro-ph.CO\]](#).
- [42] W. H. Press and P. Schechter, *Astrophys. J.* **187**, 425 (1974).
- [43] R. Barkana and A. Loeb, *Phys. Rept.* **349**, 125 (2001), [arXiv:astro-ph/0010468](#).
- [44] H. J. Mo and S. D. M. White, *Mon. Not. Roy. Astron. Soc.* **282**, 347 (1996), [arXiv:astro-ph/9512127](#).
- [45] N. Palanque-Delabrouille, C. Yèche, N. Schöneberg, J. Lesgourgues, M. Walther, S. Chabanier, and E. Armengaud, *JCAP* **04**, 038 (2020), [arXiv:1911.09073 \[astro-ph.CO\]](#).
- [46] A. Garzilli, A. Magalich, O. Ruchayskiy, and A. Boyarsky, *Mon. Not. Roy. Astron. Soc.* **502**, 2356 (2021), [arXiv:1912.09397 \[astro-ph.CO\]](#).
- [47] W. Enzi *et al.*, *Mon. Not. Roy. Astron. Soc.* **506**, 5848 (2021), [arXiv:2010.13802 \[astro-ph.CO\]](#).
- [48] B. Villasenor, B. Robertson, P. Madau, and E. Schneider, *Phys. Rev. D* **108**, 023502 (2023), [arXiv:2209.14220 \[astro-ph.CO\]](#).
- [49] P. Dayal and S. K. Giri, *Mon. Not. Roy. Astron. Soc.* **528**, 2784 (2024), [arXiv:2303.14239 \[astro-ph.CO\]](#).
- [50] M. Viel, J. Lesgourgues, M. G. Haehnelt, S. Matarrese, and A. Riotto, *Phys. Rev. D* **71**, 063534 (2005), [arXiv:astro-ph/0501562](#).
- [51] J. F. Navarro, C. S. Frenk, and S. D. M. White, *Astrophys. J.* **490**, 493 (1997), [arXiv:astro-ph/9611107](#).

- [52] N. Makino, S. Sasaki, and Y. Suto, *Astrophys. J.* **497**, 555 (1998), [arXiv:astro-ph/9710344](#).
- [53] L. Gao, S. D. M. White, A. Jenkins, C. Frenk, and V. Springel, *Mon. Not. Roy. Astron. Soc.* **363**, 379 (2005), [arXiv:astro-ph/0503003](#).
- [54] R. Barkana, *Mon. Not. Roy. Astron. Soc.* **347**, 57 (2004), [arXiv:astro-ph/0212458](#).
- [55] S. Furlanetto, *Mon. Not. Roy. Astron. Soc.* **371**, 867 (2006), [arXiv:astro-ph/0604040](#).
- [56] M. Valdes and A. Ferrara, *Mon. Not. Roy. Astron. Soc.* **387**, 8 (2008), [arXiv:0803.0370 \[astro-ph\]](#).
- [57] Z. Abdurashidova *et al.* (HERA), *Astrophys. J.* **945**, 124 (2023), [arXiv:2210.04912 \[astro-ph.CO\]](#).
- [58] A. R. Thompson, J. M. Moran, and J. Swenson, George W., *Interferometry and Synthesis in Radio Astronomy, 3rd Edition* (2017).
- [59] R. Braun, A. Bonaldi, T. Bourke, E. Keane, and J. Wagg, (2019), [arXiv:1912.12699 \[astro-ph.IM\]](#).
- [60] G. Ashton *et al.*, *Astrophys. J. Suppl.* **241**, 27 (2019), [arXiv:1811.02042 \[astro-ph.IM\]](#).
- [61] G. Ashton and C. Talbot, *Mon. Not. Roy. Astron. Soc.* **507**, 2037 (2021), [arXiv:2106.08730 \[gr-qc\]](#).
- [62] A. R. Zentner, *Int. J. Mod. Phys. D* **16**, 763 (2007), [arXiv:astro-ph/0611454](#).
- [63] T.-Y. Sun, Y. Shao, Y. Li, Y. Xu, and X. Zhang, (2024), [arXiv:2407.14298 \[astro-ph.CO\]](#).
- [64] E. Banados *et al.*, *Astrophys. J.* **909**, 80 (2021), [arXiv:2103.03295 \[astro-ph.CO\]](#).
- [65] L. Ighina, S. Belladitta, A. Caccianiga, J. W. Broderick, G. Drouart, A. Moretti, and N. Seymour, *Astron. Astrophys.* **647**, L11 (2021), [arXiv:2101.11371 \[astro-ph.GA\]](#).
- [66] A. J. Gloudemans, K. J. Duncan, A. Saxena, Y. Harikane, G. J. Hill, G. R. Zeimann, H. J. A. Röttgering, D. Yang, P. N. Best, E. Bañados, A. Drabent, M. J. Hardcastle, J. F. Hennawi, G. Lansbury, M. Magliocchetti, G. K. Miley, R. Nanni, T. W. Shimwell, D. J. B. Smith, B. P. Venemans, and J. D. Wagnveld, *Astron. Astrophys.* **668**, A27 (2022), [arXiv:2210.01811 \[astro-ph.GA\]](#).
- [67] J. Mirocha, J. B. Muñoz, S. R. Furlanetto, A. Liu, and A. Mesinger, *Mon. Not. Roy. Astron. Soc.* **514**, 2010 (2022), [arXiv:2201.07249 \[astro-ph.CO\]](#).
- [68] J. B. Muñoz, (2023), [10.1093/mnras/stad1512](#), [arXiv:2302.08506 \[astro-ph.CO\]](#).